RESEARCH PAPER

Study on the stability of compressive residual stress induced by high-frequency mechanical impact under cyclic loadings with spike loads

Hector Ruiz[1] • Naoki Osawa[1] • Sherif Rashed[2]

Abstract

In this study, the residual stress simulations of the out-of-plane gusset welded joints examined by Leitner et al. (2016) in As-welded and HFMI-treated conditions which are performed by Ruiz (2018, 2019) are reviewed and verified. Based on the reviewed simulation's results, the changes of residual stress under constant amplitude and compressive spike loads with various stress amplitudes are simulated. Sensitivity analyses of the simulation parameters in stress response simulation are carried out, and recommendations on residual stress relaxation simulation are proposed. From the residual stress relaxation simulation results, the following are found: (1) for constant amplitude cyclic loading cases, the residual stress induced by HFMI treatment shows considerable relaxation. The longitudinal component of the residual stress shows a slight increase when the maximum stress of the cyclic loading is large, about 44.5%; (2) for spike followed by constant amplitude cyclic loading cases, the residual stress shows considerable relaxation. The degree of the relaxation becomes more significant with the increase of spike load and/or the maximum stress in the constant amplitude loading except the longitudinal stress component on the top face. The longitudinal residual stress near top face shows considerable improvement showing around 21% of increment compared with the as-peened condition.

1 Introduction

The advantage of removing potential threats of the harmful tensile residual stresses (RS) and exploiting the beneficial compressive stresses by mechanical treatments is already known in the welding communities. A mechanical post-weld treatment such as high-frequency mechanical impact (HFMI) has been found to exhibit a significant fatigue life enhancement of welded joints. The effectiveness of HFMI treatment is primarily based on three effects: the local work hardening,

introduction of compressive RS and the rounded weld toe [1–11].

A concern regarding the relaxation of the RS induced by HFMI treatment has become an important topic in welding community. Measurements by Tai [12] indicated that the compressive RS was reduced just after the first loading cycle. This was confirmed by Miyashita [13] for laser peening treatment. For variable amplitude loadings, Yildirim [14] analysed the change of RS in longitudinal stiffeners made of high-strength steel, and reported that the HFMI's benefits are reduced more significantly than that for constant amplitude loadings. Hara [15] examined the fatigue strength improvement due to ultrasonic impact treatment (UIT) for ship structural members, and reported that the RS introduced by the treatment showed considerable relaxation when a large compressive load was applied, reducing the welded structure life about 35% compared with the obtained results with tensile loads.. This was confirmed by measurements in Okawa [16] showing that the compressive residual stress at the hot spot in HFMI-treated joints decreases by about 45%. Leitner et al. [17] studied the stability of HFMI-introduced RS in an out-of-plane welded joint under

✉ Hector Ruiz
  hector.ruiz@naoe.eng.osaka-u.ac.jp

1 Department of Naval Architecture and Ocean Engineering, Osaka University, Osaka, Japan

2 Joining and Welding Research Institute, Osaka University, Osaka, Japan

cyclic loadings, and showed the RS relaxation in low- and high-cyclic fatigue regions, getting up to 37% of relaxation in the longitudinal component.

It is considered that the welded joint's constraint affects the RS's relaxation. This suggests that the RS's relaxation depends not only on the stress amplitude but also on the structural detail. The applicability of the knowledge related to the relationship between RS's relaxation and loading condition to a welded joint in an actual structure has to be examined by performing a numerical (finite element, FE) RS relaxation simulations. However, the recommendations on FE meshing and choice of simulation parameters, for practical applications to ships and marine structures, has not been established yet. The objective of this study is set out best practice guidelines with respect to these simulations.

In this study, the RS simulations of the out-of-plane gusset welded joints examined by Leitner et al. [17] in As-welded and HFMI-treated conditions which are performed by Ruiz [18] are reviewed and verified. Based on those results, the changes of RS under constant amplitude (CA) and compressive spike loads with various stress amplitudes are simulated. Sensitivity analyses of the simulation parameters in stress response simulation are carried out, and recommendations on RS relaxation simulation are proposed. From the RS relaxation simulation results, the relation between RS's relaxation and the loading condition is discussed.

2 Material

For the constitutive equation, the modified Chaboche's kinematic hardening model [19], which was chosen in the previous report [18], is adopted. The yield condition is defined by Eq. (1):

$$J_2 = (\boldsymbol{\sigma} - \boldsymbol{\alpha}) = \sigma_o \tag{1}$$

where σ is the Cauchy stress tensor and α is the back-stress tensor. The development law of α is given by Eq. (2):

$$d\boldsymbol{\alpha} = \sum_{i=1}^{M} d\boldsymbol{\alpha}_i; d\boldsymbol{\alpha}_i = C_i \frac{d\varepsilon^p}{\sigma_o}(\boldsymbol{\sigma} - \boldsymbol{\alpha}) - \gamma_i \boldsymbol{\alpha}_i d\varepsilon^p \tag{2}$$

where C_i, γ_i are the material parameters, $d\varepsilon^p$ is the equivalent plastic strain increment, M is the number of kinematic hardening components and i is the component number. $M = 2$ is used in this study. σ_o is the yield stress and σ_o is given by Eq. (3), so that it can account for combined isotropic-kinematic hardening and strain rate dependency:

$$\sigma_o = \sigma_{o,0}.\mathscr{F}\left(\dot{\varepsilon}^p\right)\mathcal{G}(\varepsilon^p);$$
$$\left(\dot{\varepsilon}^p\right) = 1 + \left(\dot{\varepsilon}^p/H\right)^{1/\rho}, \ \mathcal{G}(\varepsilon^p) = 1 + a\left(\varepsilon^p\right)^b \tag{3}$$

where $\sigma_{o,0}$ is the initial yield stress, H and ρ are strain rate hardening parameters from Cowper-Symonds strain rate function and a and b are isotropic hardening parameters from Jonson-Cook Yield function.

Material parameters are the same as those adopted in [5], and are listed in Table 1. The presented material parameter was calibrated by Foehrenbach [20], by performing a single-element calculation under uniaxial load. The parameters "H" and "a" are set to large value and zero respectively to disable the isotropic part of hardening and strain rate effect (strain-rate independent pure kinematic). Chemical composition is listed in Table 2.

3 Review of the numerical study of HFMI treatment process of out-of-plane gusset welded joints [18]

3.1 Analysis target and the FE model

The simulation target is a single-sided out-of-plane gusset welded joint studied by Leitner et al. [17]. Ruiz [18] carried out numerical simulations of welding and HFMI processes. The HFMI tool is composed of a conical pin and a guide. Pin nose radius R is 2 mm. Rigid shell elements were used to model this tool. In that study, a one-half FE model was developed and simulation parameters were chosen following the recommendations of ISSC2018 V.3's benchmark report [22]. The minimum element size is $0.2 \times 0.2 \times 0.2$ mm, recommended by Ruiz [23]. The impact pitch P and indentation depth D are 0.4 mm and 0.2 mm respectively. Figure 1 shows the FE model composed of 8-node hexahedron elements. This model is adopted in the cyclic loading simulations in this study. Let "target location" be the weld toe on the main plate's centreline (see Fig. 1).

3.2 Welding process

Ruiz [18] carried out welding simulations by using the implicit thermal elastic-plastic (TEP) FE code JWRIAN [24]. The

Parameters	Values
E [GPa]	210
ν	0.3
Yield Stress σ_o [MPa]	435
C_1 [MPa]	8.9718E + 03
C_2 [MPa]	1.265488E + 04
H [1/s]	∞
$\gamma 1$	218.65
$\gamma 2$	106.98

Table 1 Material parameters used in flat sheet analyses

Table 2 Chemical composition [21]

Elements	Values (%)
C	0.22
Si	0.55
Mn	1.6
P	0.03
S	0.03

base metal is S355 steel and the filler material is G3Si1. The temperature-dependent material parameters shown in Fig. 2 were adopted. Phase transformation was neglected because in the used material it occurs at high temperature and its effect on welding RS is small. The simulation results were verified by the comparison with experimental measurements by Leitner et al. [17] and simulation result by Kim [25]. In the thermal analysis, Goldak heat source model was adopted, and the welding heat input was about 6.4 kJ/cm for both fillet and rounded seams. Welding travel speed of 1 cm/s and welding heat efficiency of 0.85 were assumed. Figure 3 shows the calculated fusion zone (the region which experienced a temperature > 1450 °C) and the macroscopy image measured in Leitner et al. [17]. The calculated fusion zone size shows a good agreement with the measured one.

3.3 HFMI treatment process

Ruiz [18] carried out HFMI treatment simulations by using explicit elastic-plastic (EEP) FE code MSC.Dytran [26]. HFMI simulations are either displacement-controlled simulations (DCS) or force-controlled simulations (FCS) [20]. Pin's impact velocity has to be prescribed in FCS, but is difficult as a matter of practice, especially for manually treated cases. Therefore, DCS is chosen in this study. For simplicity, pin is modelled as a rigid body, and it is assumed that the indentation depth and impact period are constant, USING an indentation depth D of 0.2 mm and impact pitch P equal to 0.4 mm.

As shown in Fig. 4, the out-of-plane (Z-dir.) motion was constrained at all nodes on the back face of the joint. The longitudinal (X-dir.) constraint was applied at all nodes on the symmetrical plane. The transverse (Y-Dir.) motion is prevented at only one node on the symmetrical plane. The HFMI treatment was performed only along the rounded seam (see Fig. 1).

Figure 5 shows the calculated distributions in thickness direction of RS's X-component before and after the HFMI treatment. The stresses measured in Leitner et al. [17] are also plotted in this figure. The calculated RS profiles shows reasonable agreement with the measured ones at depth < 1 mm. Over 1-mm profile is different, because X-ray diffraction was used to measure the experimental RS, wrong values could be obtained using this method away the surface. Figure 6 shows the calculated distributions in thickness direction of X-, Y- and Z-stress components and von Mises stress after the HFMI treatment. All components show high compressive values on the surface, and von Mises stress is comparable to the yield stress with consideration of strain hardening. Similar RS distribution was observed by neutron diffraction measurement in Foehrenbach et al. [20].
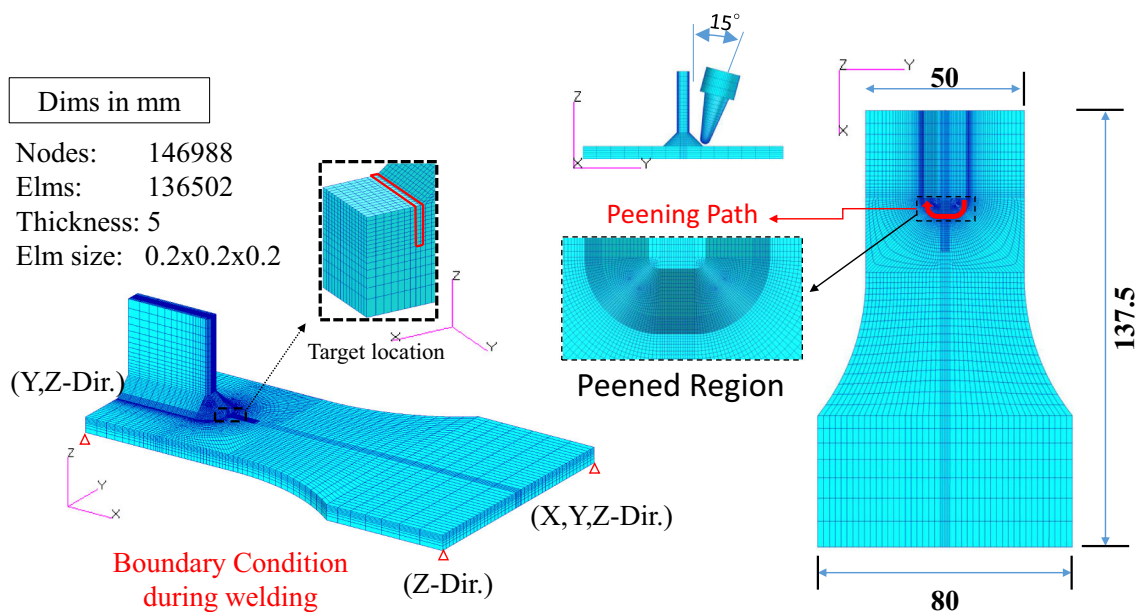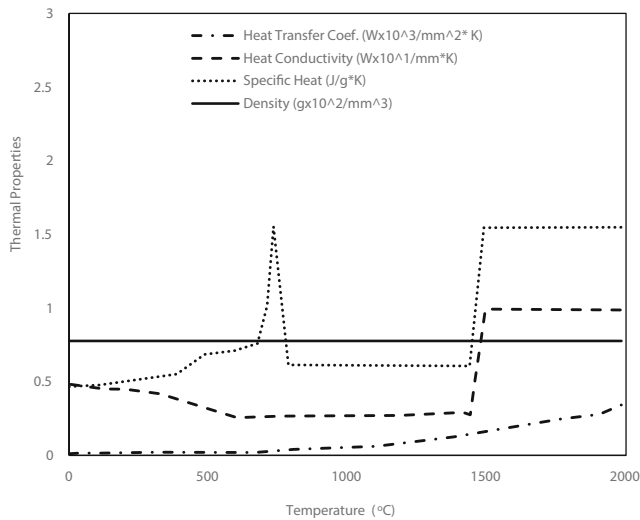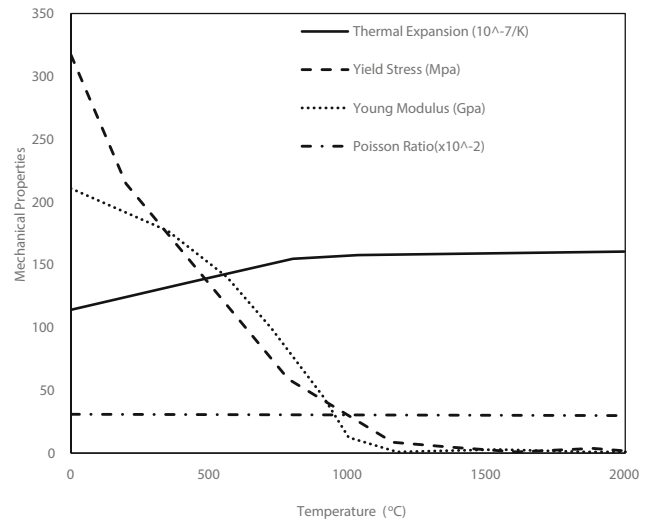

Fig. 1 The one-half FE model of the out-of-gusset welded joint for welding, HFMI and cyclic loading simulation. [18]
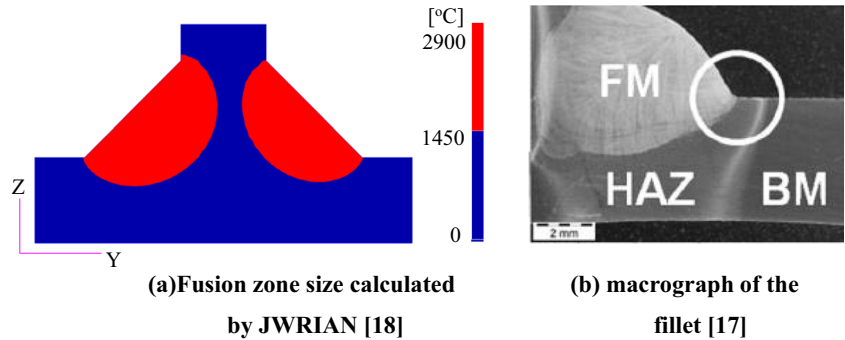
(a) Thermal Properties

(b) Mechanical Properties

Fig. 2 Temperature-dependent material properties [25]

Fig. 3 Fusion zone cross section

(a) Fusion zone size calculated by JWRIAN [18]

(b) macrograph of the fillet [17]

4 Stability of residual stress under cyclic loading

4.1 Boundary conditions

After welding and HFMI treatment simulation reviewed in Chapter 3, the changes of RS under cyclic loading conditions are simulated. As shown in Fig. 7, cyclic remote uniform stress in X-dir. is applied while the out-of-plane displacement is constrained at all nodes on the back face. Let $S_{pl,min}$ be the smallest maximum nominal stress which produces plastic deformation at the target location. Cyclic loading analyses of a stress-free model (the same FE mesh, constraint/loading conditions but without RS) are carried out in order to evaluate $S_{pl,min}$. The material parameters are the same as those adopted in the HFMI treatment simulations.
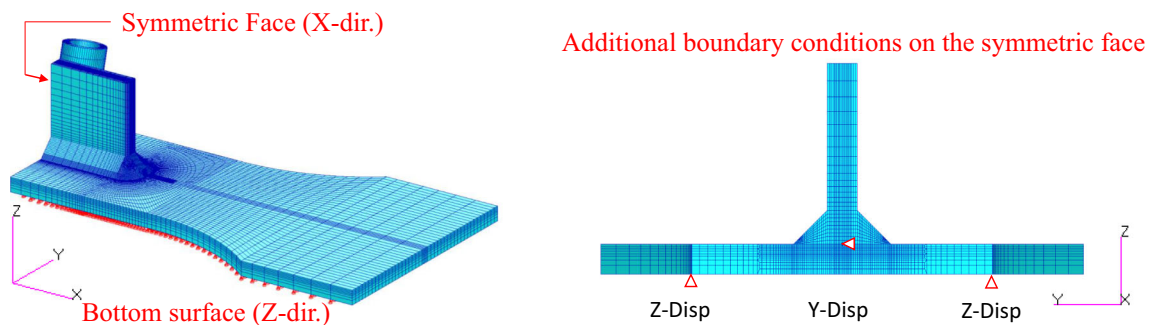

Fig. 4 The constraint conditions for HFMI treatment simulations [18]
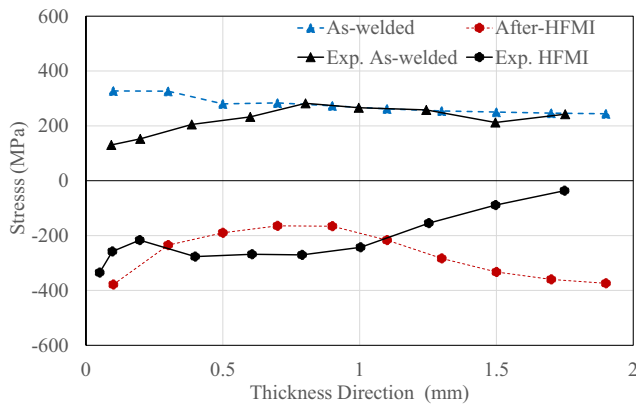
Fig. 5 The calculated distributions in thickness direction of RS's X-component at the target location before and after the HFMI treatment. (exp.: Leitner at el. [17])

Fig. 7 Boundary conditions and load condition during cyclic loading simulation.x

4.2 Constant amplitude cyclic loadings

In this section, the effect of CA cyclic loading on the RS' stability is examined. Figure 8 shows the nominal stress waveform applied to the FE model. Five cycles of constant amplitude (CA) cyclic loadings with stress ratio R of 0 are applied. Let ΔS be nominal stress range. The maximum nominal stresses, S_{max} ($=\Delta S$) are $+50$ MPa, $+75$ MPa and $+150$ MPa. Figure 9 shows the changes of equivalent plastic strain ε_p and surface stress's X-component σ_{xx} at the target location (the element facing the top face at the weld toe) of the stress-free model during constant amplitude cyclic loadings with various ΔS. The marks show ε_p and σ_{xx} at each stress reversal. It is shown that no plastic deformation occurs when $\Delta S = S_{max} = +50$ MPa and $+75$ MPa. For $\Delta S = S_{max} = +50$ MPa, finite tensile plastic deformation during the first loading can be observed, but there is almost no subsequent plastic deformation during the following cycles. These results show that $S_{pl,min}$ is not less than 75 MPa and not more than 150 MPa.
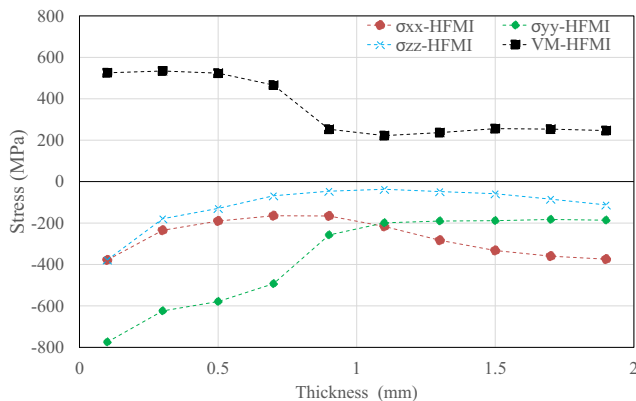

Fig. 6 The calculated distributions in thickness direction of X-, Y- and Z-components and von Mises stress of RS at the target location after the HFMI treatment. [18]
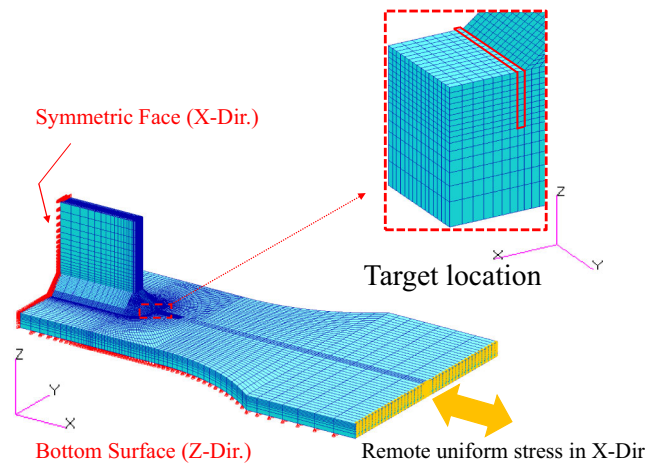
Figure 9a shows that tensile plastic strain is generated on the top face during the first tensile load only when $S_{max} > S_{pl,min}$ ($S_{max} = 150$ MPa). Upon unloading, this tensile plastic strain induces compressive residual stress, which increases the compressive RS in HFMI-treated cases, as shown in Fig. 9b.

Figures 10 shows the changes of the profiles of RS's normal X-, Y- and Z-components and von Mises stress at the target location of the HFMI-treated model after applying three CA cyclic loadings with various ΔS ($=S_{max}$) as shown in Fig. 8. The dotted lines show the as-HFMI-treated profile. The longitudinal (σ_{xx}) residual tress comparison on the top surface is shown in Fig. 11; this figure shows that the applied tensile constant amplitude loading introduces compressive (σ_{xx}) residual stress on the top surface, getting an increment of about 44.5% with $+150$ MPa. Figure 12 shows the change of the equivalent plastic strain ε_p of the element facing the top face during constant amplitude cyclic loadings. The following is shown in these figures:

X-component σ_{xx} CA loadings with $S_{max} < S_{pl,min}$ ($\Delta S = S_{max} = +50$ MPa and $+75$ MPa) have a negligible effect on the RS profiles induced by the HFMI treatment, while that with $S_{max} > S_{pl,min}$ ($\Delta S = S_{max} = +150$ MPa) causes the
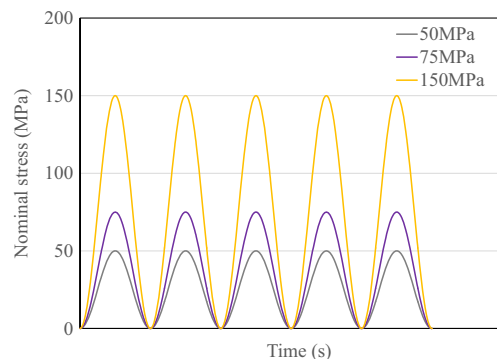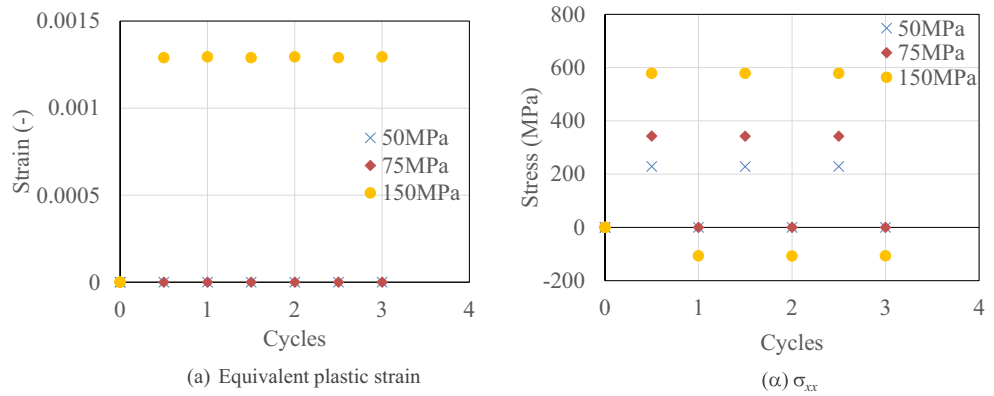

Fig. 8 Constant amplitude loading scenarios

Fig. 9 Changes of equivalent plastic strain ε_p and surface stress's X-component at the target location s_{xx} of the stress-free model during constant amplitude cyclic loadings with various stress ranges

(a) Equivalent plastic strain

(α) σ_{xx}

increase of the compressive RS on the top surface and slight decreases of those at a depth > 0.2 mm. This is due to the induced tensile plastic strain caused by a nominal tensile stress larger than $S_{pl,min}$.

Y-component σ_{yy} Relaxation of the compressive RS is observed up to a depth < 1 mm for all CA loading cases regardless of S_{max}. The decline of RS occurs even if $S_{max} < S_{pl,min}$. The decrease in RS becomes larger when S_{max} is larger.

Z-component σ_{zz} CA loadings have a negligible effect on the RS profiles regardless of S_{max}.

Von Mises stress VM Relaxation of the VM is observed up to a depth < 1 mm for all CA loading cases regardless of S_{max}. The decline of VM occurs even if $S_{max} < S_{pl,min}$. The decrease in VM becomes larger when S_{max} is larger.

Equivalent plastic strain ε_p ε_p increases during the first loading for all CA loading cases regardless of S_{max}, but there is almost no subsequent plastic deformation in following cycles. The increase in ε_p becomes larger when S_{max} is larger (0.03% for $\Delta S = S_{max} = +50$ MPa ~ 0.20% for $\Delta S = S_{max} = 150$ MPa).

In summary, for CA cyclic loading cases, it is found that the transverse stress and von Mises stress of RS show
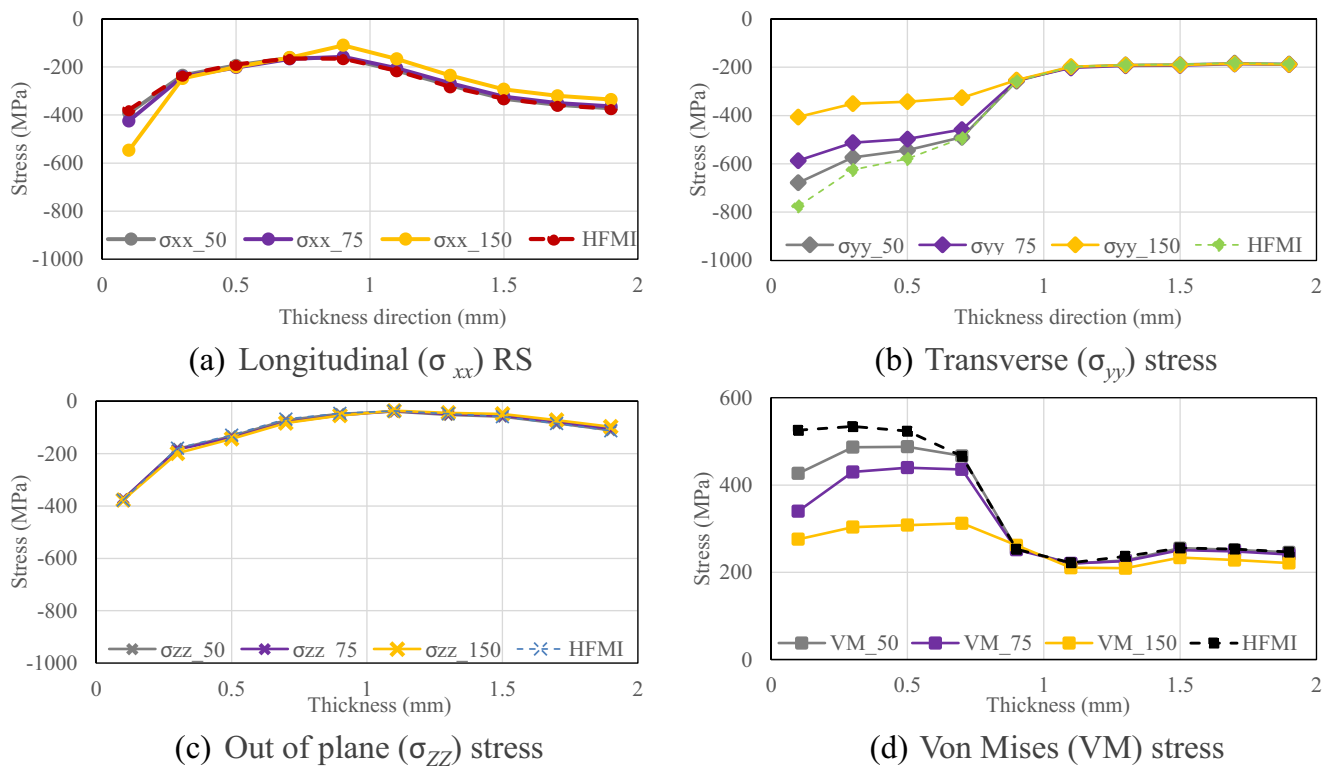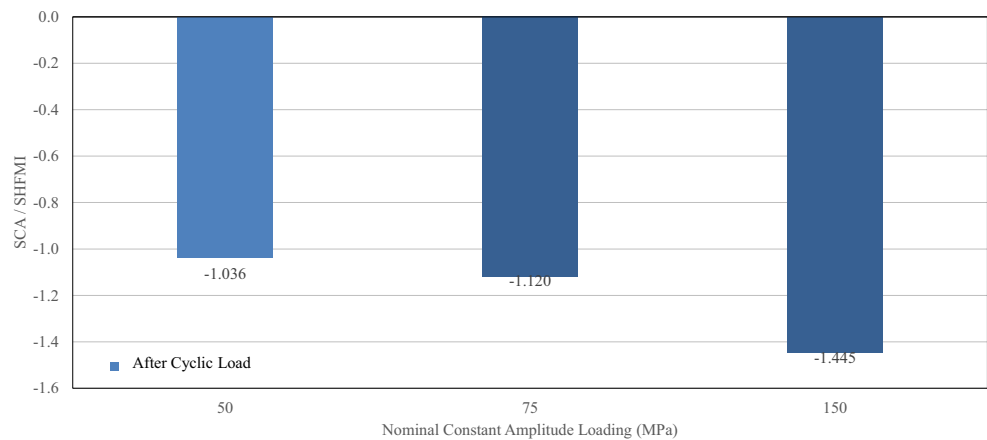
(a) Longitudinal (σ_{xx}) RS

(b) Transverse (σ_{yy}) stress

(c) Out of plane (σ_{ZZ}) stress

(d) Von Mises (VM) stress

Fig. 10 Changes of profiles of RS's normal components and von Mises stress at the target location of the HFMI-treated model during constant amplitude cyclic loadings with various stress ranges.

Fig. 11 Comparison of longitudinal (σ_{xx}) residual stress on the top surface after HFMI with that after constant amplitude loading

considerable relaxation even if $S_{max} < S_{pl,min}$, while the cyclic loading has small effects on the longitudinal and through-thickness stresses. The longitudinal compressive RS shows a slight increase for the largest S_{max}. This is due to a large tensile stress in CA cyclic loadings that causes the tensile plastic strain at the weld toe, which induces the compressive residual stress.

Under the conditions chosen, the crack face of a fatigue crack, which is at the target location, lies on the transverse plane (YZ-plane). In this case, the critical stress component is σ_{xx}. Above results show that the compressive RS in this critical direction will not deteriorate by the CA cyclic loadings examined in this study.

4.3 Cyclic loading with spike loads

In this section, the effect of a spike load and subsequent CA loading on the RS' stability is examined. Figure 13 shows an example of nominal stress waveform applied to the FE model. Since the RS relaxation due to a compressive spike load is more significant than that due to a tensile one [15, 18, 27,
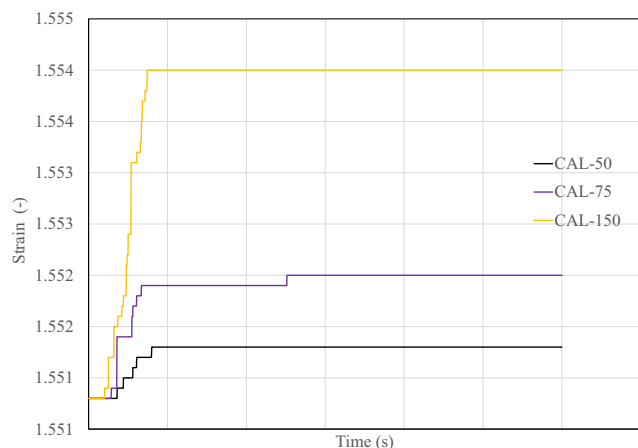
28], a compressive spike load and subsequent two cycles of CA loadings with $R = 0$ are applied. Let "spike load factor" k be defined by Eq. (4).

$$k_t |S_{min}| = k S_Y \tag{4}$$

where k_t is the stress concentration factor of 1.6, S_Y is the yield stress of 355 MPa. As shown in Table 3, four spike loads with $k = 0.75 \sim 1.36$ and two CA loadings with $\Delta S = S_{max} = 75$ and 150 MPa are applied.

Figure 14 shows the changes of the profiles of RS's normal X-, Y-, and Z-components and von Mises stress at the target location of the HFMI-treated model during the spike and CA loadings with $S_{max} = 150$ MPa ($> S_{pl,min}$). The dotted lines show the as-HFMI-treated profile. The following is shown in these figures:

X-component σ_{xx} The compressive RS is relaxed and it changes to tensile for cases with $k > 1.0$ ($|S_{min}| > 221.8$ MPa) inside of the plate (depth > 0.3 mm), and the decrease in the inside
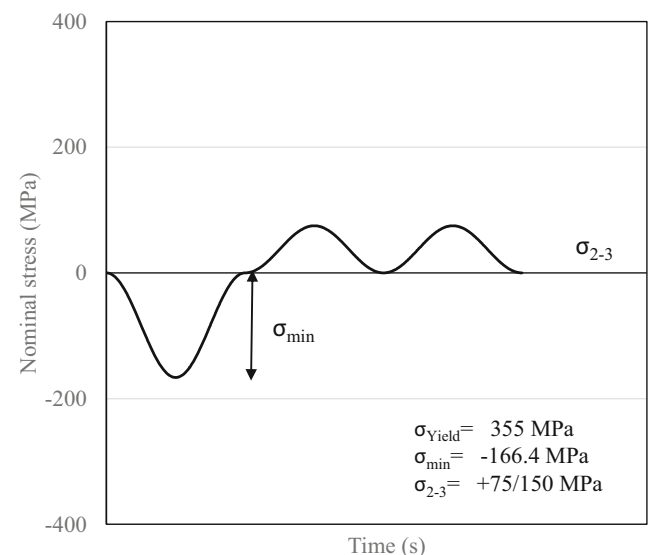

Fig. 12 Change of the equivalent plastic strain ε_p during constant amplitude cyclic loadings with various stress ranges

Fig. 13 Cyclic loading with a compressive spike load

Table 3 Material parameters used in flat sheet analyses

Scenario	Min. nominal stress (spike load) (MPa)	Spike load factor k	Nominal stress range in CA loading (MPa)
1	− 166.4	0.75	75, 150
2	− 221.8	1.00	75, 150
3	− 277.3	1.25	75, 150
4	− 301.7	1.36	75, 150

RS becomes larger when k is larger ($|S_{min}|$ is larger). In contradiction to this, the compressive RS is nearly unchanged in the top face element. It is supposed that this is due to the tensile plastic strain induced by a large tensile stress ($S_{max} = 150$ MPa $> S_{pl,min}$) applied in the CA load cycles.

Y-component σ_{yy} Relaxation of the compressive RS is calculated up to a depth < 1 mm for all loading scenarios regardless of k (S_{min}). The decrease in RS becomes larger with the increase in k, but reaches a plateau when $k > 1.0$.

Z-component σ_{zz} Spike and CA loadings have a small effect on the RS profiles regardless of k.

Von Mises stress VM Relaxation of the VM is observed up to a depth < 1 mm for all cases. The decrease in VM becomes larger when k is larger.

Figure 15 shows the changes of the profiles of RS's normal X-, Y-, and Z-components and von Mises stress at the target location of the HFMI-treated model during the spike and CA loadings with $S_{max} = 75$ MPa ($<S_{pl,min}$). The dotted lines show the as-HFMI-treated profile. The following is shown in these figures.

X-component σ_{xx} The compressive RS is relaxed over the whole range, and it changes to tensile in the centre part of the plate thickness when $k \geq 1.0$. The change in RS becomes

Fig. 14 Changes of profiles of RS's normal components and von Mises stress at the target location of the HFMI-treated model during spike and constant amplitude cyclic loadings with DS = 150 MPa
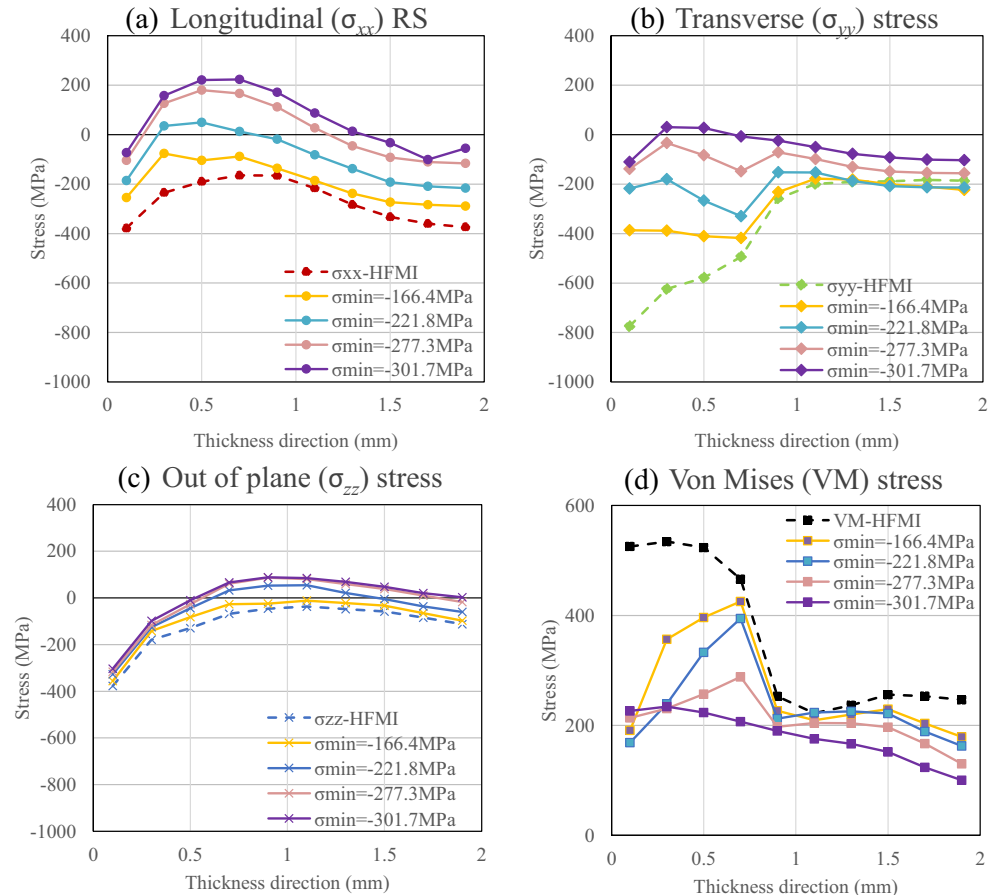
Fig. 15 Changes of profiles of RS's normal components and von Mises stress at the target location of the HFMI-treated model during spike and constant amplitude cyclic loadings with DS = 75 MPa
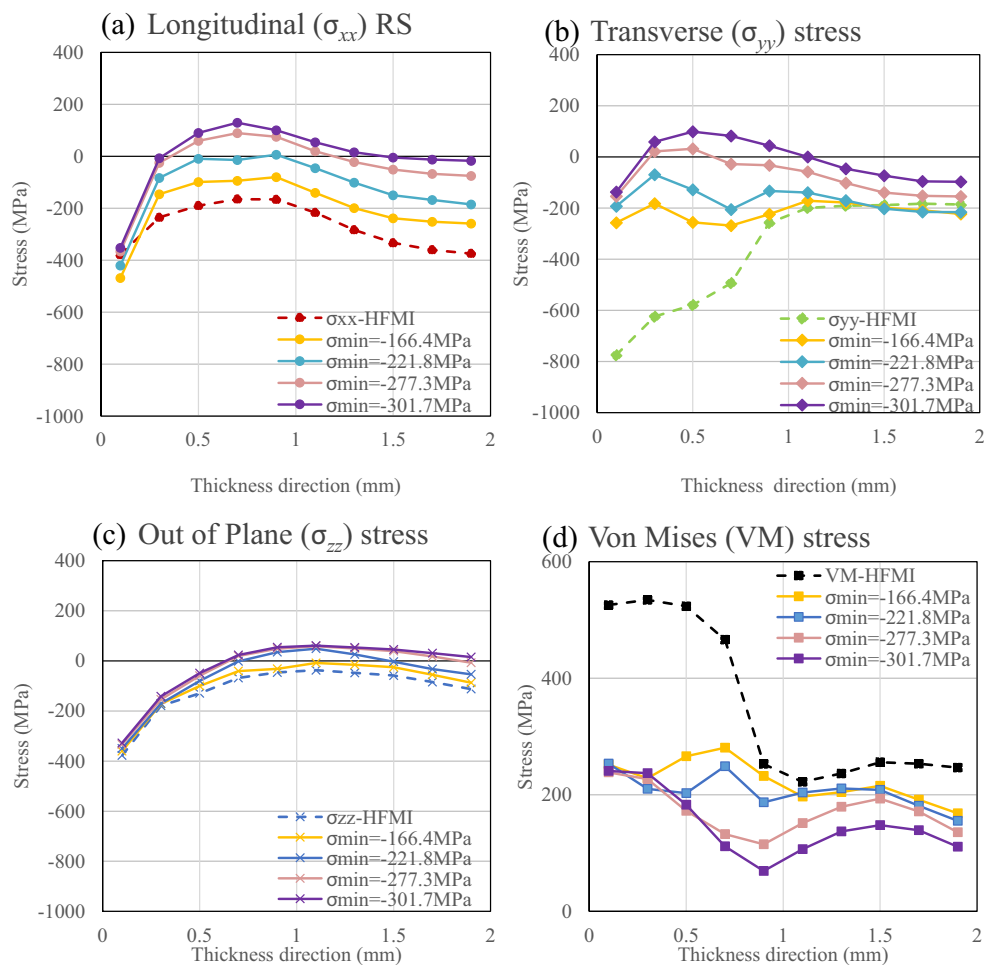

larger when k is larger ($|S_{min}|$ is larger). The reason why the top face element also shows stress relaxation, which is not observed in the case with larger S_{max} (see Fig. 14a), is that tensile plastic strain is not generated during the CA load cycles because $S_{max} < S_{pl.min}$.

Y-component σ_{yy} Relaxation of the compressive RS is calculated up to a depth < 1 mm for all loading scenarios regardless of k (S_{min}). The decrease in RS becomes larger with the increase in k, but reaches a plateau when $k > 1.0$. The change in RS is smaller than that for the case with the same k but larger S_{max} (Fig. 14b).

Z-component S_{zz} Spike and CA loadings have a small effect on the RS profiles regardless of k.

Von Mises stress VM Relaxation of VM stress is observed up to a depth < 0.8 mm for all cases. The decrease in VM stress becomes larger when k is larger. The change in VM stress is smaller than that for the case with the same k but larger S_{max} (Fig. 14d).

In summary, for spike and CA cyclic loading cases, the longitudinal and transverse components and von Mises stress of RS show considerable relaxation, while the applied load histories have negligible effects on the stress in the through-thickness direction. The degree of RS's relaxation becomes more significant with the increase of $|S_{min}|$ and/or S_{max} other than the longitudinal component on the top face. The RS's longitudinal component on the top face shows considerable change only when $S_{max} < S_{pl,min}$ because the large $S_{max}(>S_{pl,min})$ applied in the CA load cycle induces tensile plastic strain at weld toe.

Figure 16 summarizes the longitudinal (σ_{xx}) residual stress comparison on the top surface between residual stress after HFMI with that after the cyclic loading scenarios shown in Fig. 13. Figure 16a shows that the applied maximum nominal stress, $S_{max} = +150$ MPa after the compressive peak load, gives negligible relaxation of about 7% (from −378 to −352 MPa). When compressive peak loads of $S_{min} = −166.4$ MPa and $S_{min} = −221.8$ MPa are applied, compressive residual stress is introduced on the top surface, getting a maximum increase of about 20% (from −378 to −468 MPa).

Fig. 16 Longitudinal residual stress comparison on the top surface under peak load with constant amplitude

(a) Compressive peak load with constant amplitude load of + 150MPa.
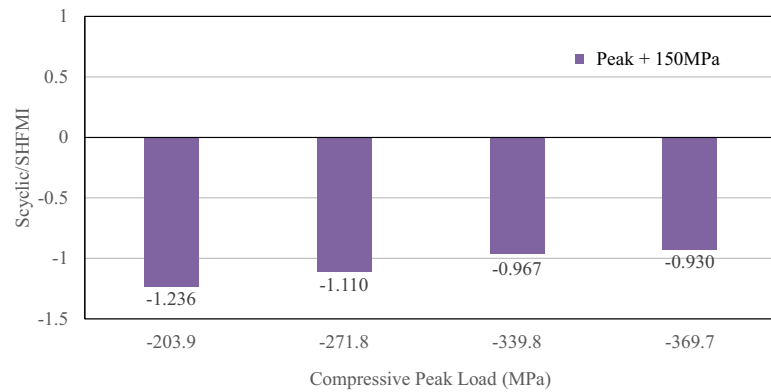
(b) Compressive peak load with constant amplitude load of +75 MPa.
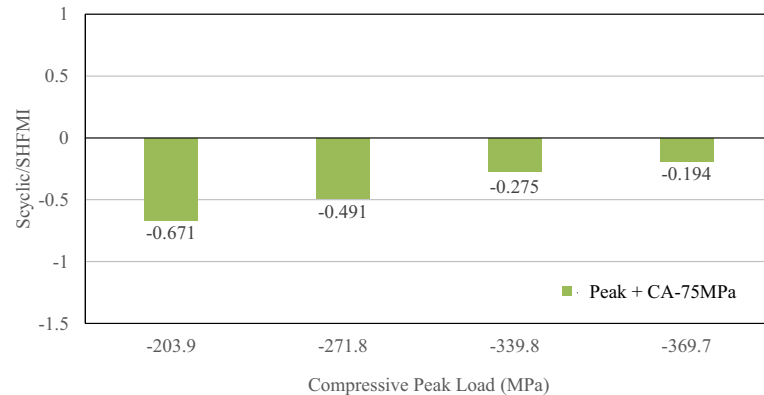
On the other hand, applying a maximum nominal stress, $S_{max} = +75$ MPa after the compressive peak load gives stress relaxation of about 32.9% (from − 378 to − 254 MPa).

5 Conclusions

In this study, the residual stress simulations for the out-of-plane gusset welded joints in As-welded and HFMI-treated conditions performed by the authors are reviewed and verified. Based on these results, the changes of residual stress under constant amplitude and compressive spike loads are simulated. From the simulation results, the following is found:

(1) For constant amplitude cyclic loading cases, the transverse component and von Mises stress of the residual stress induced by HFMI treatment show considerable relaxation even if the maximum stress is smaller than the minimum nominal stress for plastic deformation in the stress-free model, being the relaxation of about 50% and 40% near the top surface respectively, under a CA loading of + 150 MPa, while the cyclic loading has negligible effects on the stresses in the longitudinal and through-thickness directions. Only when the longitudinal component of the residual stress shows a slight increase when the maximum stress of the cyclic loading is larger than the minimum nominal stress for plastic deformation, getting an increment of 44.5%, however, through-thickness direction the different is negligible.

(2) For spike and constant amplitude cyclic loading cases, the longitudinal and transverse components and von Mises stress of the residual stress show considerable relaxation, getting relaxation of about 48.8%, 67% and 46% respectively near the top surface, when the compressive peak load of $S_{min} = − 166.4$ MPa followed by constant amplitude loading of + 150 MPa is applied, while the applied load histories have negligible effects on the stress in the through-thickness direction. The degree of the relaxation becomes more significant with the increase of spike load and/or the maximum stress in the constant amplitude loadings except the longitudinal component on the top face. The longitudinal residual stress on the top face shows considerable change only when the maximum stress of the cyclic loading is smaller than the minimum nominal stress for plastic deformation.

6 Future works

It is necessary to find out the magnitude of the loading that does not considerably deteriorate the benefits of the post-weld treatment. Furthermore, use realistic loadings conditions with variables wave amplitudes.

Due to lack of information from the literature comparison using the proper material properties and welding/HFMI/cyclic loading conditions could not be done. Therefore, it is necessary to carry out a comparison between numerical simulations with experimental measurements, where all conditions are well known.

References

1. Statnikov E, Trufyakov V, Mikheev P, Kudryavtsev Y (1996) Specification for weld toe improvement by ultrasonic impact treatment. IIW Document XIII-1617-96
2. Marquis GB, Barsoum Z (2013) A guideline for fatigue strength improvement of high strength steel welded structures using high frequency mechanical impact. Proc Eng 66:98–107
3. Yildirim HC, Marquis GB (2012) Fatigue strength improvement factors for high strength steel welded joints treated by high frequency mechanical impact. Int J Fatigue 44:168–176
4. Yildirim HC, Marquis GB, Barsoum Z (2013) Fatigue assessment of high frequency mechanical impact (HFMI) improved fillet welds by local approaches. Int J Fatigue 52:57–67
5. Marquis GB, Mikkola E, Yildirim HC, Barsoum Z (2013) Fatigue strength improvement of steel structures by high frequency mechanical impact: proposed fatigue assessment guidelines. Weld World 57:803–822
6. Marquis GB, Barsoum Z (2013) Fatigue strength improvement of steel structures by high frequency mechanical impact: proposed procedures and quality assurance guidelines. Weld World 58:19–28. https://doi.org/10.1007/s40194-013-0077-8
7. Haagensen PJ, Maddox SJ (2010) IIW recommendations on post weld improvement of steel and aluminum structures, IIW Document XIII-2200r4–07, revised February 2010
8. Mikkola E, Marquis G, Lehto P, Remes H, Hänninen H (2016) Material characterization of high-frequency mechanical impact treated high-strength steel. Mater Des 89:205–214
9. Morikage Y (2015) Improvement mechanism of fatigue strength of weld joints by hammer peening on base metal. Q J JWS 33:111–117 (in Japanese)
10. Tsutsumi S, Nagato R, Fincato R, Ishikawa T, Matsumoto R (2017) Numerical and experimental study on fatigue life extension of U-rib steel structure by hammer peening. Proc Weld Soc 35(2):169–172
11. Ishikawa Tm Matsumoto R, Tsutsumi S, Kawano H (2014) Fatigue strength improvement of rib-to-deck joints of orthotropic steel deck by peening
12. Tai M, Miki C (2012) Improvement effects of fatigue strength by burr grinding and hammer peening under variable amplitude loading. Weld World 56:109–117
13. Miyashita D (2011) Relaxation behavior of laser peening residual stressdue to mechanical loading on aluminum alloy. Trans JSME 60:617–623 (in Japanese)
14. Yildirim HC, Marquis G, Sonsino CM (2016) Lightweight design with welded high frequency mechanical impact (HFMI) treated high-strength steel joints from S700 under constant and variable amplitude loadings. Int J Fatigue 2016(91):466–474
15. Hara J, Shimoda T, Deguchi T, Mouri M, Fukuoka T, Koshio K, Kano D (2010) A study on fatigue strength improvement for ship structures by ultrasonic peening Part 1, Conference Proceedings of The Japan Association of Ship and Ocean Engineers, 2010S-G12-4 (in Japanese)
16. Okawa T, Shimanuki H, Funatsu Y, Nose T, Sumi Y (2013) Effect of preload and stress ratio on fatigue strength of welded joints improved by ultrasonic impact treatment. Weld World 57:235–241
17. Leitner M, Khurshid M, Barsoum Z (2017) Stability of high-frequency mechanical impact (HFMI) post-treatment induced residual stress states under cyclic loading of welded steel joints. Eng Struct 143:589–602
18. Ruiz H, Osawa N, Rashed S (2019) A practical analysis of residual stresses induced by high-frequency mechanical impact post-weld treatment. Weld World 63:1255–1263. https://doi.org/10.1007/s40194-019-00753-w
19. Chaboche J-L (1986) Time-independent constitutive theories for cyclic plasticity. Int J Plast 2(2):149–188
20. Foehrenbach J, Hardenacke V, Farajian M (2016) High-frequency mechanical impact treatment (HFMI) for the fatigue improvement: numerical and experimental investigations to describe the condition in the surface layers. Weld World 60(4):749–755. https://doi.org/10.1007/s40194-016-0338-4
21. American Institute of Steel and Iron (AISI) (2015) www.steel.org/, 13.11
22. Lennart J, Van Duin S, Remes H, Osawa N, Kim MH et al (2018) Committee V.3 materials and fabrication technology, proceedings of the 20th International Ship and Offshore Structures Congress (ISSC 2018). Prog Marine Sci Technol 2:143–191
23. Ruiz H, Osawa N, Murakawa H, Rashed S (2018) Stability of compressive residual stress introduced by HFMI technique, Proceeding of the ASME 2018 37th International Conference on Ocean, Offshore and Arctic Engineering. 4:V004T03A019, https://doi.org/10.1115/OMAE2018-77887
24. Ueda Y, Murakawa H, Rashwan AM, Neki I, Kamichika R, Ishiyama M, Ogawa J (1993) Development of computer aided process planning system for plate bending by line-heating (repot IV): decision making on heating conditions, location and direction (Mechanics, Strength & Structural Design). Trans JWRI 22(2):305–313
25. Kim (2017) Numerical simulation of high frequency mechanical impact (HFMI) treatment in fillet welded joints, ISSC'18 Committee V.3 Benchmark
26. MSC Software (2017) MSC DYTRAN2017 Reference Manual
27. Mikkola E, Remes H, Marquis G (2017) A finite element study on residual stress stability and fatigue damage in high-frequency mechanical impact (HFMI)-treated welded joint. Int J Fatigue 94:16–29
28. Leitner M, Ottersbock M, Pubwald S, Remes H (2018) Fatigue strength of welded and high-frequency mechanical impact (HFMI) post-treated steel joints under constant and variable amplitude loading. Eng Struct 163:215–223